Tumor-Specific Formation of Enzyme-Instructed Supramolecular Self-Assemblies as Cancer Theranostics

Peng Huang[*,†,⊥], **Yuan Gao**[*,‡,§], **Jing Lin**[†,‖], **Hao Hu**[†], **Hsien-Shun Liao**[‖], **Xuefeng Yan**[†], **Yuxia Tang**[†], **Albert Jin**[‖], **Jibin Song**[†], **Gang Niu**[†], **Guofeng Zhang**[‖], **Ferenc Horkay**[‡], and **Xiaoyuan Chen**[*,†]

[†]Laboratory of Molecular Imaging and Nanomedicine (LOMIN), National Institute of Biomedical Imaging and Bioengineering (NIBIB), National Institutes of Health, Bethesda, Maryland 20892, United States

[‡]Section on Tissue Biophysics and Biomimetics, Program on Pediatric Imaging and Tissue Sciences, Eunice Kennedy Shriver National Institute of Child Health and Human Development, National Institutes of Health, Bethesda, Maryland 20892, United States

[§]Beijing Engineering Research Center for BioNanotechnology and CAS Key Lab for Biological Effects of Nanomaterials and Nanosafety, National Center for NanoScience and Technology, No. 11 Zhongguancun Beiyitiao, Beijing 100190, China

[‖]Laboratory of Cellular Imaging and Macromolecular Biophysics, National Institute of Biomedical Imaging and Bioengineering (NIBIB), National Institutes of Health, Bethesda, Maryland 20892, United States

[⊥]Guangdong Key Laboratory for Biomedical Measurements and Ultrasound Imaging, Department of Biomedical Engineering, School of Medicine, Shenzhen University, Shenzhen 518060, China

Abstract

Despite the effort of developing various nanodelivery systems, most of them suffer from undesired high uptakes by the reticuloendothelial system, such as liver and spleen. Herein we develop an endogenous phosphatase-triggered coassembly strategy to form tumor-specific indocyanine green (ICG)-doped nanofibers (5) for cancer theranostics. Based on coordinated intermolecular interactions, 5 significantly altered near-infrared absorbance of ICG, which improves the critical photoacoustic and photothermal properties. The phosphatase-instructed coassembly process, as well as its theranostic capability, was successfully conducted at different levels ranging from *in vitro*, living cell, tissue mimic, to *in vivo*. Specifically, the tumor uptake of ICG was markedly increased to $15.05 \pm 3.78\%\,ID/g$, which was 25-fold higher than that of free ICG ($0.59 \pm 0.24\%\,ID/g$) at 4 h after intravenous injection. The resulting ultrahigh *T/N* ratios (>15) clearly differentiated tumors from the surrounding normal tissue. Complete tumor elimination with high therapeutic accuracy has been successfully achieved upon laser irradiation ($0.8\ \mathrm{W/cm^2}$, 5 min)
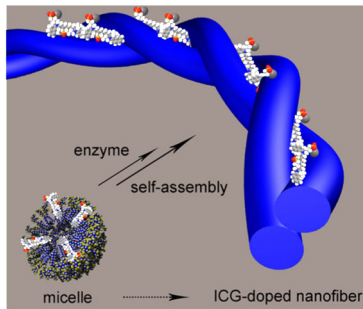
---

[*]Address correspondence to peng.huang@nih.gov, gaoy@nanoctr.cn, shawn.chen@nih.gov. .

within 24–48 h postinjection. As the first example, *in vivo* formation of tumor-specific ICG-doped nanofiber for PTT theranostics owns the immense potential for clinical translation of personalized nanomedicine with targeted drug delivery as well as for cancer theranostics.

Keywords

self-assembly; nanofibers; indocyanine green; fluorescence imaging; photoacoustic imaging; photothermal therapy; theranostics

Cancer hyperthermia treatments, which involve heating cancerous tissues/cells through external stimuli such as light, radio frequency (RF), microwave, ultrasound, or magnetic fields, have become important therapeutic modalities.[1–3] In particular, considerable interest has surrounded the utilization of photothermal therapy (PTT), due to its specific spatiotemporal selectivity and minimal invasiveness, for cancer theranostics, as PTT employs photothermal conversion agents (PTCAs) to absorb and convert optical energy into tumor-damaging heat.[4–6] However, most of the reported PTCAs have not yet been qualified for clinical implementation, which is most likely due to their poor pharmacokinetics and concerns of long-term biosafety.[7]

Using clinical agents is one of the efficient ways to develop a clinically translatable PTCA. Therefore, by screening the clinical agents approved by the Food and Drug Administration (FDA), we recognize indocyanine green (ICG; $C_{43}H_{47}N_2O_6S_2Na$, molecular weight 775) as our candidate. ICG is a near-infrared (NIR) tricarbocyanine dye which has been employed for cardiocirculatory blood flow measurements, hepatic function tests, and ophthalmic angiography in the clinic.[8–10] Due to its unique NIR absorbance/emission property (extinction coefficient $\sim 2 \times 10^5$ cm^{-1} M^{-1}) and excellent safety profile, ICG is quite promising for PTT theranostics.[11–13] However, as there are only a few reports of ICG for clinical PTT translation, the PTT application of ICG is still in the early stage.[14–16]

ICG is composed of two lipophilic polycyclic (benzoindotricarbocyanine) moieties, linked with a polymethine chain. An additional sulfonate group is extended from each polycyclic part to improve the solubility in water. The entire molecule is amphiphilic and tends to nonspecifically bind with plasma proteins, primarily albumin. After intravenous injection, the ICG molecules are exclusively taken up by hepatic parenchymal cells followed by biliary excretion,[9] which results in a very short half-life of only 2–4 min. In addition, ICG cannot actively target the tumor, which leads to a very low tumor accumulation rate.[15] Thus, it is

highly desirable to develop a strategy aiming at prolonging circulation and elevating tumor accumulation rate for tumor diagnosis and treatment.

Studies have shown that nanoparticle-based PTCAs generally exhibit longer blood circulation, higher tumor accumulation rate, and longer tumor retention time than that of free ICG, primarily due to the enhanced permeability and retention (EPR) effect.[2,7] However, the unintended uptake of nanoparticles (NPs) by the reticuloendothelial system (RES)-rich organs, including the liver and spleen, is inevitable.[17] Inspired by the abundance of protein assemblies existing in nature, small peptides with strategically designed molecular structures can self-assemble into well-defined supramolecular nanostructures (*e.g.*, micelles, nanofibers) *via* noncovalent forces, such as hydrogen bonding, π–π stacking, and hydrophobic interactions, *etc*.[18–21] Besides the numerous applications of supramolecular nanostructures demonstrated in light-harvesting[22,23] and nanofiber/protein interactions,[24–26] drug delivery is one of the most well-established categories, in which drug molecules are embedded in nanofibers for controlled release in the biological environment.[27–31]

Recently, one trend of supramolecular self-assembly focuses on the construction of assemblies *in vivo* through the regulation of specific enzymes.[32,33] This process is under dynamic control in the biological environment and the spatiotemporal distribution of resulting nanostructure responses to the targeting enzyme with abnormal activities. Thus, this new strategy makes it achievable to form the tumor-specific supramolecular self-assemblies. Meanwhile, the nature of those noncovalent forces allows the *in situ* formed nanostructures readily to incorporate ICG molecules *via* the same kind of intermolecular interactions. The accumulated ICG can discriminate cancerous tissues from noncancerous ones according to fluorescence emission, which acquires high therapeutic accuracy in cancer PTT treatment. In contrast to nanoparticle-based vehicles, this supramolecular system can easily avoid the undesired uptake of RES-rich organs while sustaining advantages including high tumor accumulation rate and long tumor retention time.

Here we report the tumor-specific enzyme-triggered coassembly of ICG (**1**) and NapFFKYp (**2**) (see molecular structures in Scheme S1) for *in vivo* cancer theranostics, in which **2** is an alkaline phosphatase (ALP)-responsive peptide. ICG could simultaneously serve as a fluorescence/photoacoustic (PA) imaging probe as well as PTCA with improved photothermal conversion efficiency.

RESULTS AND DISCUSSION

The principle for phosphatase-triggered supramolecular coassembly of ICG (**1**) and enzyme-responsive peptide precursor (**2**) is shown in Scheme 1. Figure 1a displays the schematic conversion of micelles to nanofiber in the presence of enzyme. The coassembly mechanism traps ICG along the nanofibers by head-to-tail arrangement (*J*-aggregates). Initially, the simple mixing of **1** and **2** in a ratio of 1:50 led to the micelle structure, as shown in Figure 1b. The hydrodynamic diameters of **2** and **2** + **1** measured by the dynamic light scattering method were 209.6 ± 28.6 and 203.9 ± 19.0 nm, respectively (Figure 1g). After the addition of ALP, the tyrosine phosphorus ester on **2** was hydrolyzed by the dephosphorylation reaction. The resulting hydrogelators (**3**) were capable of incorporating molecule **1** into

nanofibers **5**. As shown in Figure 1c, **5** has well-defined fibrous structures. To determine the effect of the incorporation of **1** into nanofibers, we made a thorough comparison between the nanofibers without (**4**) and with (**5**) ICG *via* transmission electron microscopy (TEM) (Figures S1–S3) or atomic force microscopy (AFM) (Figure 1d–f). The double helix structure of **4** was clouded with the incorporation of **1** (Figures S1–S3). The heights of **4** and **5**, measured from AFM images, were 13.7 and 12.8 nm, respectively (Figure 1h). The height decrease may be attributed to the tight intermolecular packing of **1** and **2**. To verify the structural stability of **5**, we tried to determine the release rate of **1** from the nanofibers in water or phosphate-buffered saline (PBS) solutions. When **5** was dialyzed in water or PBS at 37 °C, no appreciable loss of absorption was observed, which indicated the excellent stability of **5**.

The optical property of **5** is the basis for biophotonic imaging and therapy.[2] The formation of **5** was monitored by time-course measurements of the UV–vis spectra in Figure 2a. At the beginning of the dephosphorylation reaction, the absorption of the mixture of **1** and **2** consisted of a strong peak at 780 nm and a weak shoulder at 707 nm corresponding to the dimeric (*H*-like aggregate) and monomeric forms of ICG. A clear bathochromic and hyperchromic shift appeared from 780 to 808 nm with time, which suggested the transition from ICG monomers to its *J*-aggregates. The remarkably red-shifted, narrower and stronger NIR absorption peak makes **5** highly promising as PTCA for PTT. With the increase of aging time from 1 to 24 h, the surface of the nanofibers also becomes more smooth (Figure 2b–e).

Meanwhile, the morphological changes among **1**, **2**, and **5** were also investigated by circular dichroism (CD) spectropolarimetry (Figure 2f). **1** showed no special peak in the range of 190–500 nm. **2** had a negative peak near 190 nm and two positive peaks around 200 and 217 nm. After the formation of nanofibers, **5** had a positive peak near 195 and a negative peak near 215 nm, which are the characteristic peaks for a *β*-sheet structure. In addition, the appearance of a positive peak at 408 nm can only be allocated to the coassembly of **1** and **2**. As shown in Figure 2g, the intensity of the peak at 408 nm gradually increases and arrives at a plateau at around 50 μg/mL of **1**, which suggests the maximum loading of mole ratio is 1:2 (**1/2**). The results confirm the phosphatase-triggered coassembly of **2** and **1** with high efficiency.

The optical densities of **1** and **5** in the solutions were also recorded in Figure 2h and Figure S4, which indicated a significant increase of OD at 808 nm with the formation of a nanofiber. When the concentration of **1** was 10 or 20 μg/mL, the OD at 808 nm of **5** was about 2.4- or 2.6-fold higher than that of **1**, respectively. To evaluate the cellular phosphatase-triggered coassembly of **1** and **2**, we selected cellular phosphatase overexpressing HeLa cells as a model and measured their OD at 808 nm *versus* the incubation time. As shown in Figure 2i, for the group treated with **1** only, the average OD quickly increased within 1 h, and then reached a plateau in 1–4 h. At the presence of the phosphatase inhibitor (5 μmol/L CinnGEL 2Me in 0.1% DMSO),[34] the average OD grew slowly within 1 h and then reached a similar plateau as the previous group. In contrast, the average OD change of the group of HeLa cells with the formation of **5** was distinct from

both groups above and exhibited a continual increase of intensity within 4 h. More interestingly, there was an increase in the peak of OD 808 nm at 1 h, indicating the successful coassembly of **1** and **2**, along with the transition of **1** from monomers to *J*-aggregates as illustrated *in vitro*. The OD changes at 780 nm were also recorded in Figure S5. The formation of **5** in HeLa cells was also evidenced by cell TEM images (Figure S6).[35] Beyond the demonstration of the coassembly of **1** and **2** at the cellular level, we also verified this process in a tissue mimic environment (Figure S7).

Figure 3a illustrates the *in vivo in situ* conversion of micelles to nanofibers after intravenous (i.v.) injection. After i.v. administration, the injected micelles gradually accumulate within the tumor site by EPR effect. As described before, with the overexpression of endogenous phosphatase, **2** will be efficiently converted to the corresponding hydrogelator **3**, which was able to self-assemble into nanofibers at certain concentration *in situ*. The micelles that did not form nanofibers will dissociate and be rapidly cleared. The fluorescence properties of **1** and **5** were carefully investigated both *in vitro* and *in vivo*. ICG exhibits an emission peak at around 820 nm, making it highly suitable for NIR fluorescence imaging with deeper tissue penetration and minimal background autofluorescence interference. In Figure 3b, the fluorescence intensity of **1** was partially quenched with the formation of a nanofiber. We also observed a time-dependent quenching of **1** on HeLa cells incubated with **1** and **2**, while the cells incubated with **1** showed no fluorescence intensity decrease within 3 h (Figure 3c). These results suggested that **1** was successfully incorporated into the nanofiber both *in vitro* and in living cells.

To investigate the feasibility of *in situ* enzyme-triggered self-assembly, mice bearing a HeLa tumor were used. When the tumors reached 60 mm³, the mice received intravenous injection of either **1** or **1** + **2** (**1**, 10 mg/kg; **2**, 100 mg/kg). NIR fluorescence imaging was recorded by a Maestro II *in vivo* imaging system (Figures 3d and S8). For the group treated with **1** + **2**, the whole-body distributed fluorescence signal was observed at the very beginning stage due to the existence of abundant ICG monomers. Over time, the intensity of the fluorescence signal at the tumor site continually increased, which made the tumor clearly differentiable from the surrounding normal tissues as early as 1 h postinjection (p.i.). Over 24 h, only the tumor sustained a relatively strong fluorescence signal, which lasted for the following 2 weeks (Figure S8). In contrast, in the group of mice treated with **1** only, a major portion of **1** was quickly taken up by liver within 30 min and excreted quickly *via* the biliary system within 4 h, which was in agreement with previous studies.[14,15] The similar result was observed on 4T1-tumor-bearing mice after the same treatment (Figure S9). More interestingly, by intratumoral administration of **1** + **2**, the overwhelming majority of ICG held the tumor fort, while free ICG was totally flushed out *via* blood circulation within 2 days (Figure S10).

To verify the *in situ* tumor-specific formation of **5** without the uptake of RES-rich organs, we harvested the major organs of mice for *ex vivo* imaging at 24 h (Figure 3e). We found tumor tissues only in the group with the formation of **5** showing a strong fluorescence signal, and there was nontraceable residue of **1** in other organs. In contrast, tumor tissues from the group treated with **1** only showed a very weak fluorescence signal. Both the *in vivo* and *ex*

vivo results coincided with the assumption that the formation of nanofibers *in vivo* was tumor-specific and the incorporation of **1** into nanofibers was effcient.

According to the semiquantification of fluorescence signals in Figure 3d, we compared the *T/N* ratio in Figure 3f. At 30 min p.i., the *T/N* ratio in the group with **5** was 14.98 ± 3.02, which was about 2-fold higher than that of the group treated with **1** (7.46 ± 1.5). The contrast in fluorescence imaging reached the maximum at 4 h p.i. (*T/N* ~ 19.3) and decreased slightly afterward. Thus, the tumors can be easily differentiated from the surrounding normal tissues with ultrahigh *T/N* ratios (>15) starting from 1 to 24 h. In contrast, the *T/N* ratio from the group treated with **1** can only reach as high as 8 and subsides to 1 swiftly.

To better understand the *in vivo* performance of **1** with the existence of **2**, we also studied the pharmacokinetics of **1** (Figure 3g). According to the fluorescence signal, the blood circulation half-life of **1** in the presence of **2** was 1.63 h, which was significantly longer than that of **1** without **2** (2–4 min).[13] Quantitatively, we extracted **1** from tumors at 4 or 24 h p.i. and measured the fluorescence emission intensity to determine the accumulation of **1** (Figure 5f). With the existence of **2**, the uptake of **1** at the tumor site markedly increased to $15.05 \pm 3.78\%ID/g$, which was 25-fold higher than that of without **2** ($0.59 \pm 0.24\%ID/g$) at 4 h p.i.

To verify that the formation of supramolecular self-assembly was tumor-specific, the phosphatase inhibitor (50 μL, 10 μmol/L CinnGEL 2Me in 0.1% DMSO) was intratumorally injected for 3 days (once a day) before treatment to suppress the activity of phosphatase in HeLa tumor tissues (Figure 3i). The addition of the inhibitor did not make an observable difference at the early time points, which implied that the early accumulation was mostly likely due to the EPR effect. However, at 24 h p.i., the fluorescence signal of the tumors without inhibitor was 2.9-fold higher than that of the tumors injected with phosphatase inhibitor. This difference strongly suggested that the *in situ* formation of nanofibers was controlled by the active phosphatase. The absence of sufficient phosphatase activity would not initiate the formation of nanofibers, and a major portion of **1** was flushed out *via* blood circulation. These results suggested that the *in situ* self-assembly takes place at specific tumors with overexpressed phosphatase.

The PA spectra of **1** and **5** are shown in Figure 4a. **5** represents a narrow peak at 808 nm, while **1** gives a broad shoulder in the range of 720–840 nm. Therefore, we chose 808 nm as the suitable excitation wavelength for the comparison of PA imaging. The PA densities of **1** and **5** at 808 nm are compared in Figure 4b, which indicated a significant increase of PA signal with the formation of nanofiber. When the concentration of **1** is 10 or 20 μg/mL, the PA signal at 808 nm of **5** is about 2.32- or 2.07-fold higher than that of **1**, respectively.

For *in vivo* tumor PA imaging studies, we investigated the same animal model used in the NIR fluorescence imaging. The *in vivo* 2D and 3D cross-sectional ultrasonic and PA images of the tumor area were taken at different time points after intravenous injection upon 808 nm excitation (Figure 4c). The PA signal of **5** was much stronger than that of **1** at all the time points examined. Semiquantification of PA signals in the tumor area revealed that the

average tumor PA intensity (3.54 ± 0.24 au at 4 h or 3.39 ± 0.81 au at 24 h) of **5** was *ca.* 5.8 times higher than that of **1** (0.61 ± 0.03 au at 4 h or 0.58 ± 0.02 au at 24 h) (Figure 4d). Complementary to the observation from fluorescence imaging, these PA results further strengthened our assumption that the *in situ* formation of **5** significantly improved the tumor accumulation rate of **1**.

To investigate the light-to-heat conversion ability, we measured the temperature elevation of **1** and **5** in aqueous solutions with the same exposure conditions (808 nm, 1 W/cm^2, 3 min). We found a significantly enhanced photothermal conversion efficiency of **5** over **1** at either 10 or 20 μg/mL of **1** (Figure 5a). Then we examined the *in vitro* cytotoxicity and PTT efficacy of **5** on HeLa cells with **1** as the control. To determine the cytotoxicity, the viabilities of HeLa or 4T1 cells incubated with various concentrations of **5** (**1**, 10 μg/mL; **2**, 0–500 μg/mL) for 24 h without laser irradiation were evaluated (Figures S11 and S12). **5** showed negligible toxicity at all tested concentrations, which suggested that **5** was quite biocompatible. Light-induced PTT efficacy was assessed on HeLa cells by CCK-8 assay (Figure 5b) and live/dead cell staining kit (Figure 5c), respectively. Without laser irradiation, both **1** and **5** exhibited negligible toxicity. With laser irradiation, it was reasonable that **5** and **1** displayed a laser dose-dependent cytotoxicity to HeLa cells. However, the PTT efficacy of **5** was always higher than that of **1** under the same exposure, which suggested the improved photothermal conversion efficiency of **5** over **1**. Calcein AM (green) and PI (red) costaining was used to differentiate the live and dead cells after PTT treatment. Almost no cell death was found in the control, laser only, and **5** only groups according to the live/dead staining (Figure 5c). While the group of cells with the formation of **5** received laser irradiation for 5 min, all cells within the laser spot were killed, with the appearance of an intense homogeneous red fluorescence, leaving the cells outside the laser spot alive. These results suggested that the success of phosphatase-triggered coassembly of **1** and **2** to form **5** with improved PTT efficiency in the cell level.

Based on the previous fluorescence and PA imaging results, two time points (24 and 48 h p.i.) were selected as the suitable time points to implement PTT treatment. Mice bearing HeLa and 4T1 tumors were used as the animal models. When the tumors reached 60 mm^3, the mice were intravenously administered **1** + **2** (**1**,5 mg/kg; **2**, 100 mg/kg, *n* = 5) or **1** (**1**, 5 mg/kg, *n* = 5). An infrared thermal camera was used to monitor the temperature increase for *in vivo* thermal imaging (Figure 5d,e). No obvious temperature change was observed in the PBS control group. With the formation of **5**, the temperature at the tumor site increased by 21.7 (24 h p.i.) or 16.3 °C (48 h p.i.) after 5 min laser irradiation (808 nm, 0.8 W/cm^2). As shown in Figure 5f, the tumor with **5** was effectively ablated; a black scar was left at the original tumor site, and no reoccurrence was observed. The *in vivo* NIR fluorescence imaging can be used to monitor the treatment response (Figure S13), due to the photobleaching property of ICG. The tumor growth curve (Figure 5g) also indicated that all the tumors with **5** were effectively ablated at day 2 without reoccurrence regardless the PTT treatment applied at 24 or 48 h p.i. In contrast, all the tumors in other groups grew at a similar speed. We also found that the group of mice that received **5** and PTT treatment had greatly prolonged survival over 60 days, without a single death (Figure 5h). Mice in control

groups had to be sacrificed on day 26 due to the extensive tumor burden. The similar treatment effect was obtained on 4T1-tumor-bearing mice (Figures S14 and S15).

Hematoxylin and eosin staining of tumor sections were collected from several different groups of mice at 2 h after laser irradiation (Figure S16). We found significant cancer cell damage with nuclear membrane fragmentation and nuclei shrinkage with karyorrhexis and pyknosis in the group receiving both **5** and laser irradiation. No cancer cell damage was observed in the other groups. No obvious damage or inflammation was observed in other major organs including the hearts, livers, spleens, lungs, and kidneys, as compared to the control groups (Figure S16).

Literature reported PTCAs mainly include small organic NIR dyes such as ICG, noble metal NPs (*e.g.*, Au, Ag, Pd, Pt, and Ge), carbon-based nanomaterials, and so on.[36–38] Statistically, NPs show better a PTT effect compared with small NIR dyes.[1] However, the poor clearance and high RES–organ accumulation of NPs hinder their clinical translation. Small NIR dyes with low molecular weight can be excreted shortly after systemic administration, without concerns for their long-term toxicity. Therefore, the combination of the advantages of small NIR dyes and NPs may lead to a solution for clinical translatable PTCAs.

The tumor-specific conversion of micelles to nanofibers is dependent on overexpressed enzyme activity. During the morphology conversion between the nanostructures, the clinical agent ICG was spontaneously integrated into the nanofiber *in situ*. The 1D nanofiber structure traps ICG along the nanofibers by head-to-tail arrangement (*J*-aggregates), which may delocalize coherent π-electrons and result in a transition to a lower energy level.[39,40] The *J*-aggregate formation of ICG shows a narrowed, red-shifted, and enhanced NIR absorption that is critical to the improvement of photoacoustic and photothermal properties. The fluorescence of ICG was partially quenched during the formation of the nanofiber. Based on the fact that the input photons were converted to either fluorescence emission or thermal energy, in our case, the enhanced absorption and decreased fluorescence of ICG promise better photothermal conversion efficiency and photoacoustic response. In addition, the OD and fluorescence associated with the formation of ICG-doped nanofiber may serve as a useful and more sensitive indicator than hydrogelation to determine and report the trajectory of nanofiber formation during coassembly progress.

The *in situ* tumor-specific formation of nanofibers can avoid the risk of ICG uptake/retention in RES-rich organs and enhance the total accumulation, retention, and cell uptake of ICG in tumors. To avoid the risk of undesired damage to normal tissues near lesions and to improve the therapeutic accuracy, the best PTT implementation time is in the range of 24–48 h postinjection, allowing the residual accumulation of ICG micelles in other normal tissues to be dissociated and cleared. Meanwhile, fluorescence and PA imaging can be used to monitor of treatment response.

CONCLUSION

In conclusion, we have developed an *in situ* tumorspecific formation of enzyme-instructed supramolecular self-assemblies to enrich FDA-approved agent ICG for fluorescence/

photoacoustic dual-modality imaging-guided PTT. Due to the intermolecular interaction between peptide and ICG, ICG molecules are spontaneously doped into nanofibers by head-to-tail arrangement, namely, *J*-aggregates, which induce the red shift and significantly enhanced NIR absorption of ICG. The ICG-doped nanofiber shows enhanced NIR absorbance, partially quenched fluorescence emission, and unique photoacoustic and photothermal properties. The cancer theranostic capability of ICG–nanofiber was carefully investigated both *in vitro* and *in vivo*. The *in situ* tumor-specific formation of NPs can efficiently avoid the uptake/retention by RES and simultaneously improve tumor accumulation and retention. This study is important not only because it provides a novel concept of *in situ* tumor-specific formation of NPs that can potentially be applied to deliver diagnostic/therapeutic agents, avoid the risk of unintended uptake/retention in RES-rich organs, and enhance the total tumor accumulation and retention but also because it paves the way toward the goal of personalized medicine by endogenous stimuli-instructed construction of functional nanostructures for clinical translatable PTT theranostics or guidance of surgical resection.

EXPERIMENTAL SECTION

Nanofiber Formation

ICG (10 μg/mL) and NapFFKYp peptide (0.1–1 mg/mL) were codissolved into PBS (pH 7–8). Alkaline phosphatase (1 U) was then added to start the formation of the ICG-doped nanofiber. The nanofiber without ICG was used as the control. A Genesys 10S UV–vis spectrophotometer (Thermo Scientific, Waltham, MA) was used to monitor formation progress with quartz cuvettes with an optical path of 1 cm. To assess the stability of **5**, **5** (**1** and **2** in a ratio of 1:50) was dialyzed in PBS and water at 37 °C. The released ICG was calculated by using the ICG UV calibration curve at 780 nm.

In Vivo Fluorescence Imaging

HeLa-tumor-bearing mice were intravenously injected with either **1** or **1** + **2** (**1**, 10 mg/kg; **2**, 100 mg/kg, $n = 4$). Fluorescence images were acquired by a Maestro II *in vivo* imaging system (Caliper Life Sciences, Hopkinton, MA) at 0.5, 1, 2, 4, 24, 48, and 168 h postinjection. Excitation filter is from 710 to 760 nm. Emission filter is a 800 nm long-pass. Acquisition range is 780 to 590 nm (10 nm steps). To analyze the biodistribution of ICG, the mice were sacrificed at 24 h postinjection. Tumors and other major organs were collected for *ex vivo* fluorescence imaging.

In Vivo Photoacoustic Imaging

HeLa-tumor-bearing mice received intravenous injection with either **1** or **1** + **2** (**1**, 10 mg/kg; **2**, 100 mg/kg, $n = 4$). Photoacoustic imaging was performed by a Vevo 2100 LAZR system (VisualSonics Inc. New York, NY) equipped with a 40 MHz, 256-element linear array transducer on tumors. Excitation wavelength was fixed at 808 nm.

In Vivo Photothermal Imaging

Thermal images were captured by a SC300 infrared camera (FLIR, Arlington, VA). The images were analyzed by Examin IR image software (FLIR). The excitation source was an

808 nm diode-pumped solid-state laser system (LASERGLOW Technologies, Toronto, Canada). Thermal images of HeLa-tumor-bearing mice were taken at 24 and 48 h p.i. (**1** at 5 mg/kg, and **2** at 100 mg/kg, $n = 5$) with exposure to 808 nm laser irradiation (0.8 W/cm^2, 5 min).

In Vivo PTT Cancer Treatment

HeLa-tumor-bearing mice were randomly divided into seven groups with five animals per group to determine tumor growth rate, including (1) untreated mice (control), (2) mice with PBS administration and laser irradiation (PBS + laser), (3) mice with **5** administration (**5** only), (4) mice with **1** administration and laser irradiation (**1** + laser), (5) mice with **2** administration and laser irradiation (**2** + laser), (6) mice with **5** administration and laser irradiation at 24 h p.i. (**5** + laser 24 h p.i.), and (7) mice with **5** administration and laser irradiation at 48 h p.i. (**5** + laser 48 h p.i.). The same tumor exposure (808 nm, 0.8 W/cm^2, 5 min) was used in all treatment experiments. The tumor sizes were measured by a caliper every other day after treatment. Tumor volume (V) was calculated by the following equation: $V = AB^2 \times 0.5$, where A was the longer and B was the shorter diameter (mm). The relative tumor volumes were normalized to their initial sizes. For PTT treatment of 4T1-tumor-bearing mice, we used a protocol the same as that used with HeLa-tumor-bearing mice.

Supplementary Material

Refer to Web version on PubMed Central for supplementary material.

Acknowledgment

REFERENCES AND NOTES

1. Thakor AS, Gambhir SS. Nanooncology: The Future of Cancer Diagnosis and Therapy. Ca-Cancer J. Clin. 2013; 63:395–418. [PubMed: 24114523]

2. Lovell JF, Jin CS, Huynh E, Jin H, Kim C, Rubinstein JL, Chan WC, Cao W, Wang LV, Zheng G. Porphy-some Nanovesicles Generated by Porphyrin Bilayers for Use as Multimodal Biophotonic Contrast Agents. Nat. Mater. 2011; 10:324–332. [PubMed: 21423187]

3. Huang X, El-Sayed IH, Qian W, El-Sayed MA. Cancer Cell Imaging and Photothermal Therapy in the Near-Infrared Region by Using Gold Nanorods. J. Am. Chem. Soc. 2006; 128:2115–2120. [PubMed: 16464114]

4. Huang X, Jain PK, El-Sayed IH, El-Sayed MA. Plasmonic Photothermal Therapy (PPTT) Using Gold Nanoparticles. Lasers Med. Sci. 2008; 23:217–228. [PubMed: 17674122]

5. Huang P, Rong P, Lin J, Li W, Yan X, Zhang MG, Nie L, Niu G, Lu J, Wang W, et al. Triphase Interface Synthesis of Plasmonic Gold Bellflowers as Near-Infrared Light Mediated Acoustic and Thermal Theranostics. J. Am. Chem. Soc. 2014; 136:8307–8313. [PubMed: 24842342]

6. Hirsch LR, Stafford RJ, Bankson JA, Sershen SR, Rivera B, Price RE, Hazle JD, Halas NJ, West JL. Nanoshell-Mediated Near-Infrared Thermal Therapy of Tumors under Magnetic Resonance Guidance. Proc. Natl. Acad. Sci. U. S. A. 2003; 100:13549–13554. [PubMed: 14597719]

7. Huang P, Rong P, Jin A, Yan X, Zhang MG, Lin J, Hu H, Wang Z, Yue X, Li W, et al. Dye-Loaded Ferritin Nanocages for Multimodal Imaging and Photothermal Therapy. Adv. Mater. 2014; 26:6401–6408. [PubMed: 25123089]

8. Vinegoni C, Botnaru I, Aikawa E, Calfon MA, Iwamoto Y, Folco EJ, Ntziachristos V, Weissleder R, Libby P, Jaffer FA. Indocyanine Green Enables Near-Infrared Fluorescence Imaging of Lipid-Rich, Inflamed Atherosclerotic Plaques. Sci. Transl. Med. 2011; 3:84ra45.

9. Bahmani B, Bacon D, Anvari B. Erythrocyte-Derived Photo-Theranostic Agents: Hybrid Nano-Vesicles Containing Indocyanine Green for Near Infrared Imaging and Therapeutic Applications. Sci. Rep. 2013; 3:2180. [PubMed: 23846447]

10. Desmettre T, Devoisselle JM, Mordon S. Fluorescence Properties and Metabolic Features of Indocyanine Green (ICG) as Related to Angiography. Surv. Ophthalmol. 2000; 45:15–27. [PubMed: 10946079]

11. Kanazaki K, Sano K, Makino A, Takahashi A, Deguchi J, Ohashi M, Temma T, Ono M, Saji H. Development of Human Serum Albumin Conjugated with Near-Infrared Dye for Photoacoustic Tumor Imaging. J. Biomed. Opt. 2014; 19:96002. [PubMed: 25191833]

12. Sheng Z, Hu D, Zheng M, Zhao P, Liu H, Gao D, Gong P, Gao G, Zhang P, Ma Y, et al. Smart Human Serum Albumin-Indocyanine Green Nanoparticles Generated by Programmed Assembly for Dual-Modal Imaging-Guided Cancer Synergistic Phototherapy. ACS Nano. 2014; 8:12310–12322. [PubMed: 25454579]

13. Yan L, Qiu L. Indocyanine Green Targeted Micelles with Improved Stability for Near-Infrared Image-Guided Photothermal Tumor Therapy. Nanomedicine (London, U. K.). 2015; 10:361–373.

14. Zhao P, Zheng M, Yue C, Luo Z, Gong P, Gao G, Sheng Z, Zheng C, Cai L. Improving Drug Accumulation and Photothermal Efficacy in Tumor Depending on Size of ICG Loaded Lipid-Polymer Nanoparticles. Biomaterials. 2014; 35:6037–6046. [PubMed: 24776486]

15. Zheng M, Zhao P, Luo Z, Gong P, Zheng C, Zhang P, Yue C, Gao D, Ma Y, Cai L. Robust ICG Theranostic Nanoparticles for Folate Targeted Cancer Imaging and Highly Effective Photothermal Therapy. ACS Appl. Mater. Interfaces. 2014; 6:6709–6716. [PubMed: 24697646]

16. Yang H, Mao H, Wan Z, Zhu A, Guo M, Li Y, Li X, Wan J, Yang X, Shuai X, et al. Micelles Assembled with Carbocyanine Dyes for Theranostic Near-Infrared Fluorescent Cancer Imaging and Photothermal Therapy. Biomaterials. 2013; 34:9124–9133. [PubMed: 24008037]

17. Huynh E, Leung BY, Helfield BL, Shakiba M, Gandier JA, Jin CS, Master ER, Wilson BC, Goertz DE, Zheng G. *In Situ* Conversion of Porphyrin Microbubbles to Nanoparticles for Multimodality Imaging. Nat. Nanotechnol. 2015; 10:325–332. [PubMed: 25822929]

18. Gao Y, Zhao F, Wang Q, Zhang Y, Xu B. Small Peptide Nanofibers as the Matrices of Molecular Hydrogels for Mimicking Enzymes and Enhancing the Activity of Enzymes. Chem. Soc. Rev. 2010; 39:3425–3433. [PubMed: 20623068]

19. Yang Z, Liang G, Xu B. Enzymatic Hydrogelation of Small Molecules. Acc. Chem. Res. 2008; 41:315–326. [PubMed: 18205323]

20. Cui H, Webber MJ, Stupp SI. Self-Assembly of Peptide Amphiphiles: From Molecules to Nanostructures to Biomaterials. Biopolymers. 2010; 94:1–18. [PubMed: 20091874]

21. Cui H, Muraoka T, Cheetham AG, Stupp SI. Self-Assembly of Giant Peptide Nanobelts. Nano Lett. 2009; 9:945–951. [PubMed: 19193022]

22. Sugiyasu K, Fujita N, Shinkai S. Visible-Light-Harvesting Organogel Composed of Cholesterol-Based Perylene Derivatives. Angew. Chem., Int. Ed. 2004; 43:1229–1233.

23. Channon KJ, Devlin GL, MacPhee CE. Efficient Energy Transfer within Self-Assembling Peptide Fibers: A Route to Light-Harvesting Nanomaterials. J. Am. Chem. Soc. 2009; 131:12520–12521. [PubMed: 19678637]

24. Gao Y, Long MJ, Shi J, Hedstrom L, Xu B. Using Supramolecular Hydrogels to Discover the Interactions between Proteins and Molecular Nanofibers of Small Molecules. Chem. Commun. (Cambridge, U. K.). 2012; 48:8404–8406.

25. Zhang X, Chu X, Wang L, Wang H, Liang G, Zhang J, Long J, Yang Z. Rational Design of a Tetrameric Protein to Enhance Interactions between Self-Assembled Fibers Gives Molecular Hydrogels. Angew. Chem., Int. Ed. 2012; 51:4388–4392.

26. Javid N, Roy S, Zelzer M, Yang Z, Sefcik J, Ulijn RV. Cooperative Self-Assembly of Peptide Gelators and Proteins. Biomacromolecules. 2013; 14:4368–4376. [PubMed: 24256076]

27. Ehrbar M, Schoenmakers R, Christen EH, Fussenegger M, Weber W. Drug-Sensing Hydrogels for the Inducible Release of Biopharmaceuticals. Nat. Mater. 2008; 7:800–804. [PubMed: 18690239]

28. Gao Y, Kuang Y, Guo ZF, Guo Z, Krauss IJ, Xu B. Enzyme-Instructed Molecular Self-Assembly Confers Nanofibers and a Supramolecular Hydrogel of Taxol Derivative. J. Am. Chem. Soc. 2009; 131:13576–13577. [PubMed: 19731909]

29. Li J, Gao Y, Kuang Y, Shi J, Du X, Zhou J, Wang H, Yang Z, Xu B. Dephosphorylation of D-Peptide Derivatives to Form Biofunctional, Supramolecular Nanofibers/Hydrogels and Their Potential Applications for Intracellular Imaging and Intratumoral Chemotherapy. J. Am. Chem. Soc. 2013; 135:9907–9914. [PubMed: 23742714]

30. Cheetham AG, Zhang P, Lin YA, Lock LL, Cui H. Supramolecular Nanostructures Formed by Anticancer Drug Assembly. J. Am. Chem. Soc. 2013; 135:2907–2910. [PubMed: 23379791]

31. Zhang P, Cheetham AG, Lin YA, Cui H. Self-Assembled TAT Nanofibers as Effective Drug Carrier and Transporter. ACS Nano. 2013; 7:5965–5977. [PubMed: 23758167]

32. Gao Y, Shi J, Yuan D, Xu B. Imaging Enzyme-Triggered Self-Assembly of Small Molecules inside Live Cells. Nat. Commun. 2012; 3:1033. [PubMed: 22929790]

33. Liang G, Ren H, Rao J. A Biocompatible Condensation Reaction for Controlled Assembly of Nanostructures in Living Cells. Nat. Chem. 2010; 2:54–60. [PubMed: 21124381]

34. Zhu S, Bjorge JD, Fujita DJ. PTP1B Contributes to the Oncogenic Properties of Colon Cancer Cells through Src Activation. Cancer Res. 2007; 67:10129–10137. [PubMed: 17974954]

35. Gao Y, Berciu C, Kuang Y, Shi J, Nicastro D, Xu B. Probing Nanoscale Self-Assembly of Nonfluorescent Small Molecules inside Live Mammalian Cells. ACS Nano. 2013; 7:9055–9063. [PubMed: 24067160]

36. Cheng L, Wang C, Feng L, Yang K, Liu Z. Functional Nanomaterials for Phototherapies of Cancer. Chem. Rev. 2014; 114:10869–10939. [PubMed: 25260098]

37. Huang P, Lin J, Li W, Rong P, Wang Z, Wang S, Wang X, Sun X, Aronova M, Niu G, Leapman RD, Nie Z, Chen X. Biodegradable Gold Nanovesicles with an Ultrastrong Plasmonic Coupling Effect for Photoacoustic Imaging and Photothermal Therapy. Angew. Chem., Int. Ed. 2013; 52:13958–13964.

38. Zhang Z, Wang J, Chen C. Near-Infrared Light-Mediated Nanoplatforms for Cancer Thermo-Chemotherapy and Optical Imaging. Adv. Mater. 2013; 25:3869–3880. [PubMed: 24048973]

39. Wurthner F, Kaiser TE, Saha-Moller CR. *J*-Aggregates: From Serendipitous Discovery to Supramolecular Engineering of Functional Dye Materials. Angew. Chem., Int. Ed. 2011; 50:3376–3410.

40. Kim OK, Je J, Jernigan G, Buckley L, Whitten D. Super-Helix Formation Induced by Cyanine *J*-Aggregates onto Random-Coil Carboxymethyl Amylose as Template. J. Am. Chem. Soc. 2006; 128:510–516. [PubMed: 16402838]
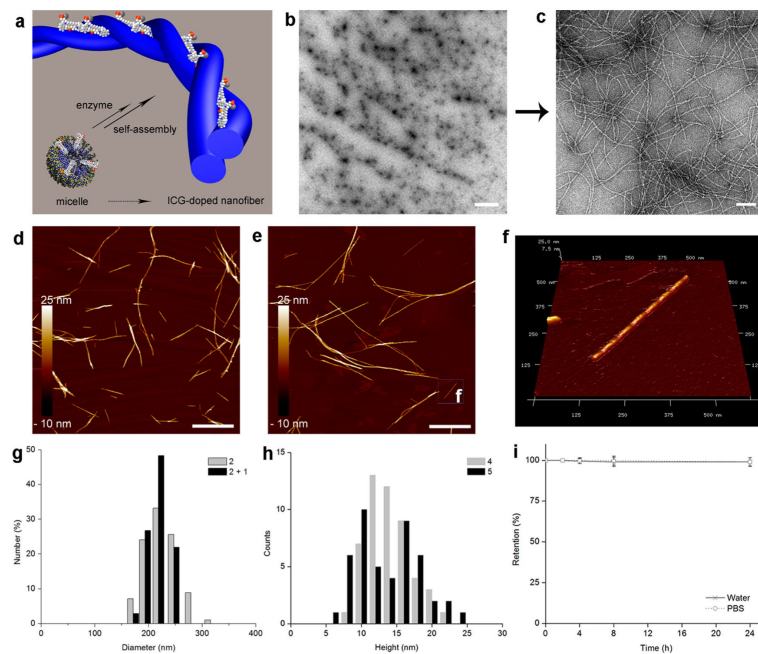
Figure 1.
Enzyme-triggered self-assembly of ICG-doped nanofiber 5 in solution. (a) Schematic conversion of micelles to nanofiber *via* an enzyme-catalyzed dephosphorylation. TEM images of the negatively stained (b) micelles (scale bar: 1 μm) and (c) 5 (scale bar: 100 nm). AFM images of (d) 4 and (e,f) 5 (scale bars: 1 μm). (g) Size distributions of 2 and 2 + 1 measured by dynamic light scattering. (h) Height histograms of 4 and 5 determined from AFM images. (i) Retention of 5 dialyzed in water or PBS at 37 °C. Data are presented as mean ± SD ($n = 3$).
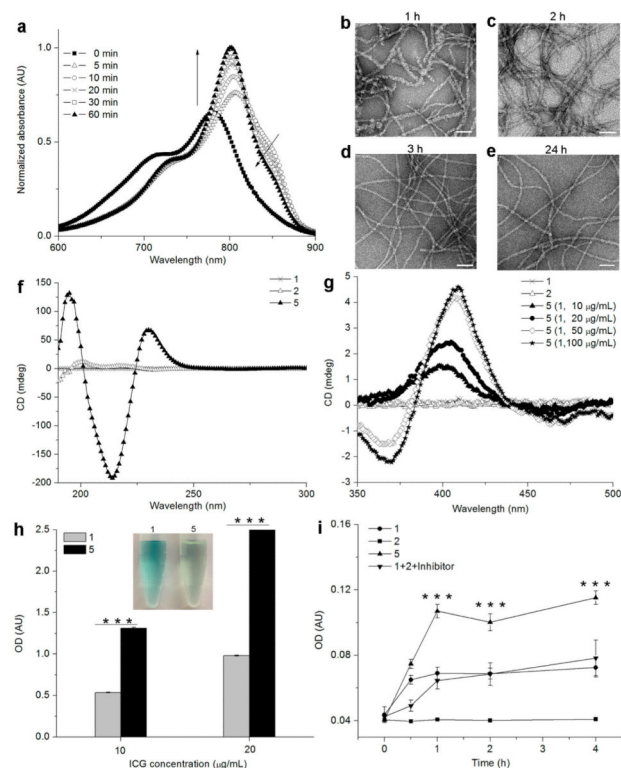
Figure 2.
Optical property and structure conformations of 5. (a) Time-course UV–vis spectra of 5 during ALP-catalyzed process. (b–e) TEM images of 5 at different aging time points. (f) CD spectra of 1, 2, and 5. (g) CD spectra of 5 with different concentrations of 1 (2, 100 μg/mL). (h) Optical density (OD) changes at 808 nm of 1 and 5 at different ICG concentrations (1 and 2 in a ratio of 1:100). The inset is the corresponding photograph of 1 at 10 μg/mL. ***P < 0.001. (i) OD changes at 808 nm of cellular phosphatase-triggered self-assembly on HeLa cells incubated with different samples (1, 10 μg/mL; 2, 500 μg/mL). ***P < 0.001.
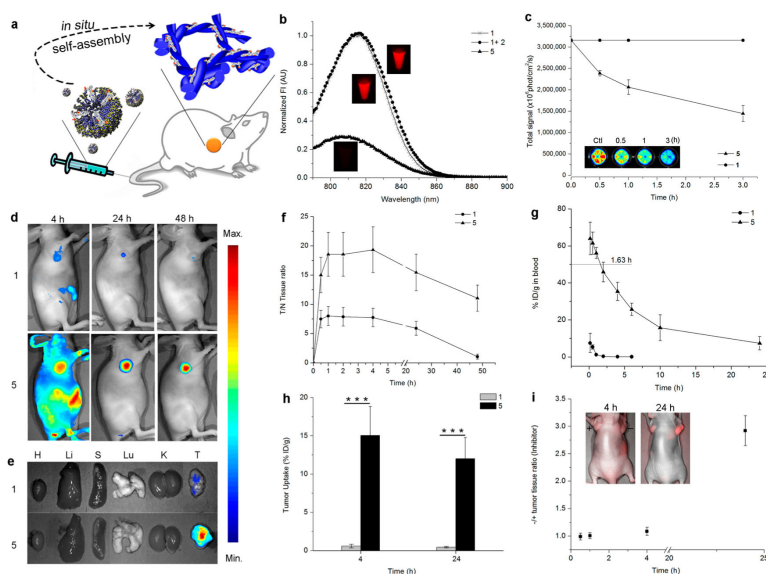
Figure 3.

In vivo in situ enzyme-triggered self-assembly of 5 monitoring by fluorescence imaging. (a) Scheme of *in situ* conversion of micelles to nanofiber after intravenous injection. (b) Fluorescence spectra of 1, 1 + 2, and 5 (1 and 2 in a ratio of 1:100; the insets are corresponding fluorescence images). (c) Fluorescence intensity changes of HeLa cells incubated with 1 (1, 10 μg/mL) and 5 (1, 10 μg/mL; 2, 500 μg/mL; inset is corresponding fluorescence image). (d) Representative NIR fluorescence images of 5 (1, 10 mg/kg; 2, 100 mg/kg, $n = 4$) and 1 (1, 10 mg/kg, $n = 4$) on HeLa-tumor-bearing mice after intravenous administration. Images were acquired at 4, 24, and 48 h postinjection (p.i.). (e) *Ex vivo* NIR fluorescence images of tumor tissues and major organs collected at 24 h p.i. ($n = 4$). (f) *T/N* ratio after intravenous injection of 1 or 1 + 2 (5) as a function of time. Data are presented as mean $\pm$ SD ($n = 4$). (g) Blood circulation curves of 1 or 1 + 2 (5) in mice after intravenous injection determined based on ICG fluorescence in the blood lysates. Data are presented as mean $\pm$ SD ($n = 4$) (h) Tumor ICG uptake of 1 or 5 in HeLa-tumor-bearing nude mice 4 or 24 h after injection (%ID g^{-1} = percentage of the injected dose per gram of tissue). The ICG content was determined by the ICG fluorescence from diluted tissue lysates. Data are presented as mean $\pm$ SD ($n = 4$). ***$P < 0.001$. (i) NIR fluorescence intensity ratio of tumor tissues without or with phosphatase inhibitor. The insets are corresponding fluorescence images. Data are presented as mean $\pm$ SD ($n = 4$).
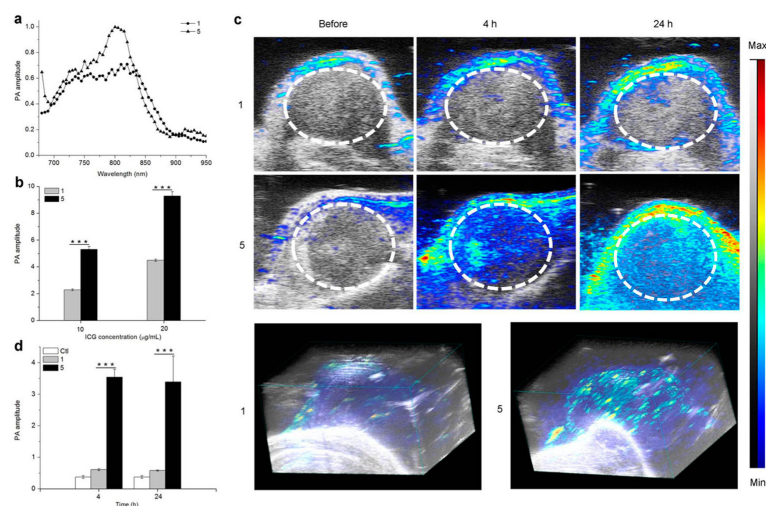
Figure 4.

In vivo in situ enzyme-triggered self-assembly of 5 monitored by photoacoustic imaging. (a) PA spectra of 1 and 5. (b) PA intensity changes of 1 and 5 at different ICG concentrations (1 and 2 in a ratio of 1:100). ***$P < 0.001$. (c) Representative 2D and 3D PA images of 1 (1, 10 mg/kg, $n = 4$) and 5 (1, 10 mg/kg; 2, 100 mg/kg, $n = 4$) on HeLa tumor tissues at 4 or 24 h p.i. The red circles indicate the region of interest in the tumors. (d) PA intensities of tumor tissues at 4 or 24 h p.i. ***$P < 0.001$.
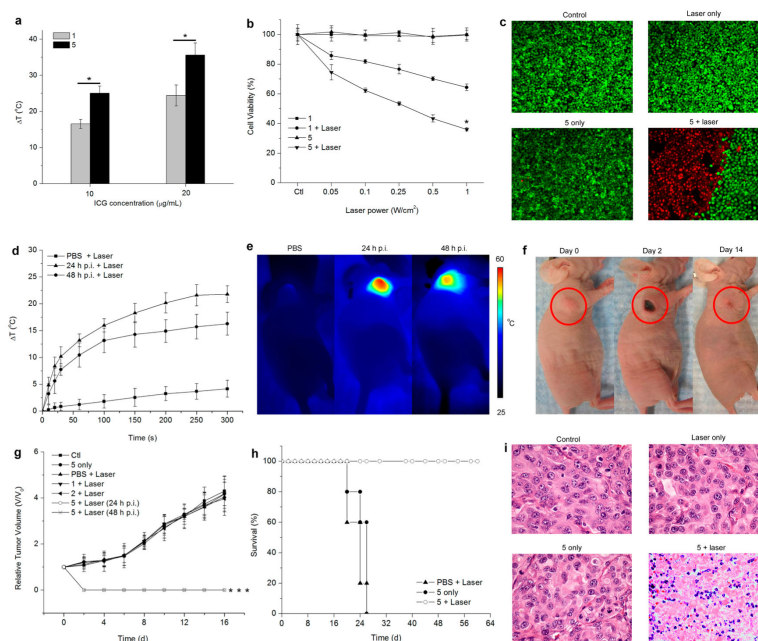
Figure 5.
Photothermal effects of *in situ* enzyme-triggered self-assembly of 5. (a) Heat generation ability of 1 and 5 in aqueous solutions (1 and 2 in a ratio of 1:100, 808 nm laser irradiation, 1 W/cm^2, 3 min). *P< 0.05. (b) Relative viabilities of HeLa cells incubated with 1 (1, 10 μg/mL) and 5 (1, 10 μg/mL; 2, 500 μg/mL) for 4 h with or without 808 nm laser irradiation (0.05–1 W/cm^2, 3 min). *P< 0.05. (c) Calcein AM and PI costaining of HeLa cells incubated with 1 and 5 for 4 h with or without 808 nm laser irradiation (1 W/cm^2, 5 min). (d) Heating curves of HeLa tumors upon laser irradiation as a function of irradiation time. (e) Thermal images of HeLa tumor-bearing mice at 24 and 48 h p.i. (1 at 5 mg/kg, and 2 at 100 mg/kg) with exposure to 808 nm laser irradiation (0.8 W/cm^2, 5 min). (f) Photographs of HeLa-tumor-bearing mice at different days after PTT treatment. (g) Tumor growth curves of different groups of HeLa-tumor-bearing mice after PTT treatment. Tumor volumes have been normalized to their initial sizes. Error bars represent the standard deviations of five mice per group. ***P< 0.001. (h) Survival curves of the HeLa tumor mice after various treatments. (i) Hematoxylin and eosin staining of tumor sections collected from different groups of mice.
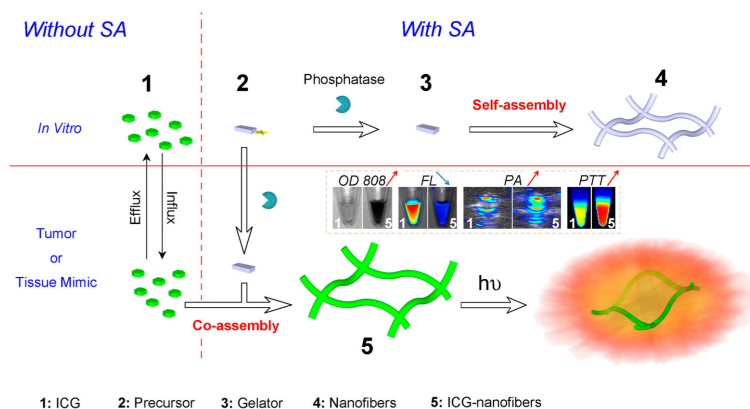
Scheme 1.

Principle for enzyme-triggered supramolecular coassembly of 1 and 2. *In vitro*: Precursor 2 is converted to hydrogelator 3 *via* dephosphorylation catalyzed by ALP. These hydrogelators self-assemble in water to form nanofibers 4. Tumor or tissue mimic: 2 is catalyzed by a cellular phosphatase into 3, which is able to coassemble with 1 and form ICG-doped nanofibers 5. Within 5, 1 takes the *J*-aggregate arrangement, which is evidenced by the red-shifted and significantly enhanced absorbance. 5 shows partially self-quenched fluorescence and enhanced photoacoustic and photothermal signals. However, without self-assembly, 1 is excreted shortly *via* efflux pump. Upon laser irradiation, 5 can efficiently convert photons into tumor-damaging heat.